Indian Journal of Engineering & Materials Sciences
Vol. 3, August 1996, pp. 141-147

Estimation of shock-cell structure of axisymmetric supersonic free jets

R C Mehta[a]* & J K Prasad[b]

[a]Aerodynamics Division, [b]Aerothermal Test Facility Division
Vikram Sarabhai Space Centre, Trivandrum 695 022, India

Received 12 October 1995; accepted 15 April 1996

Numerical and experimental results on the supersonic free jets issuing from convergent-divergent conical nozzles of different Mach numbers are presented. In the numerical calculations, the two-stage Runge-Kutta time-stepping scheme is applied assuming inviscid and axially symmetric flow while in the experiments, the flow field was visualized using Schlieren photography and static pressures along the centre line of the free jets are measured using static probe. Effects of exit Mach number and expansion ratio on shock-cell structure are studied with the help of Schlieren pictures, isobar contours and velocity vector plot. A linear relationship between shock cell length and β^2 is obtained for exit Mach numbers of 2.2, 2.6 and 3.1 and expansion ratio in the range 1.2-0.4.

An understanding of the shock-cell structure of free jet flow field is essential in order to understand aeroacoustic behaviour where the shock contributes significantly to jet noise. Therefore, numerical and experimental studies are required to predict shock-cell structure of the underexpanded and overexpanded axisymmetric supersonic free jets emanating from convergent-divergent nozzles.

An extensive experimental investigation have been carried out on the axisymmetric jets exhausting from sonic and supersonic nozzles into still surrounding and also into supersonic stream[1] and a semi-empirical expressions has been presented for calculation of first shock-cell length. Cheng and Chow[2] have applied method of characteristic in conjunction with shadowgraph pictures to locate Mach disk in supersonic free jet and jet structure. Tam, Jackson and Seiner[3] have developed analytical method to compute shock-cell length which is based on a linear solution for the shock-cell structure employing the method of multiple-scale asymptotic expansion. However, the numerical models are more useful for quantitative predictions particularly nonlinear problems. Abdel-Fattah[4] has reported the measured shock-cell lengths for supersonic free jets issuing from conical convergent-divergent nozzle obtained from Schlieren pictures.

The different numerical analysis have found that near flow field structure for highly underexpanded and overexpanded jets are dominated by inviscid processes[5,6]. The numerical solution of unsteady Euler equations to obtain flow field of underexpanded two-dimensional free jets was also carried out by using finite difference method[7]. An extensive numerical studies of underexpanded jets have been made[8]. Zeeuw and Powell[9] have made Euler calculation of axisymmetric underexpanded jets by an adaptive-refined method. They noticed that the location of the Mach disk is sensitive to the jet Mach number. These numerical studies of free jets reveal that the time-marching method can capture the flow field features of free jets.

The above literature survey reveals that numerical and experimental approaches are the common aerodynamic tool to investigate complex problems. The present study addresses the computational flow visualization of the supersonic free jets coming out from conical convergent-divergent nozzles. The primary objectives are to provide an efficient numerical procedure for the solution of the Euler equations and to compare the predicted results with the experimental data. The static pressure distributions along the jet axis are measured and have been compared with the numerical results. The first and second shock-cell lengths are measured from Schlieren pictures and isobar contours.

Numerical Method

The equations solved are the axisymmetric Euler equations describing the flow of an inviscid and compressible fluid. To capture shocks and discontinuities, the Euler equations are written in conservation form as:

*Author to whom correspondence should be addressed

$$\frac{\partial \mathbf{U}}{\partial t}+\frac{\partial \mathbf{F}}{\partial x}+\frac{1}{r}\frac{\partial (r\mathbf{G})}{\partial r}+\frac{\mathbf{H}}{r}=0 \qquad \ldots (1)$$

where

$$\mathbf{U}=\begin{bmatrix}\rho\\ \rho u\\ \rho v\\ \rho e\end{bmatrix},\ \mathbf{F}=\begin{bmatrix}\rho u\\ \rho u^2+p\\ \rho vu\\ (\rho e+p)\,u\end{bmatrix}$$

$$\mathbf{G}=\begin{bmatrix}\rho v\\ \rho uv\\ \rho v^2+p\\ (\rho e+p)\,v\end{bmatrix},\ \mathbf{H}=\begin{bmatrix}0\\ 0\\ p\\ 0\end{bmatrix} \qquad \ldots (2)$$

The specific total energy e is defined relative to the specific energy I and fluid velocity components by

$$e=I+\frac{1}{2}(u^2+v^2) \qquad \ldots (3)$$

Finally, an equation of state is specified to relate the flow variables to the static pressure as

$$p=\rho I(\gamma-1) \qquad \ldots (4)$$

Numerical Formulations

An integral form of Eq. (1), over a finite volume fixed in time is:

$$r_c\frac{\partial}{\partial t}\int_\Omega \mathbf{U}d\Omega+\int_\Gamma \bar{r}(\mathbf{F}dr-\mathbf{G}dx)+\int_\Omega \mathbf{H}d\Omega=0 \qquad \ldots (5)$$

where Ω refers to the volume with boundary Γ, r_c is the centroid of the cell and $\bar{r}$ is the average cell radius. The computational domain is divided into a finite numer of quadrilateral cells. The conservative variables within each cell are calculated by their average value at the cell centre and such quantities are denoted by suffices (i,j). A system of ordinary differential equations have been obtained by applying Eq. (5) separately to each cell. These equations have the form:

$$r_c\Delta A_{i,j}\frac{d(\mathbf{U}_{i,j})}{dt}+\mathbf{Q}(\mathbf{U}_{i,j})-\mathbf{D}(\mathbf{U}_{i,j})=0 \qquad \ldots (6)$$

where ΔA is the cell volume, and $\mathbf{Q}$ represents the net absolute flux out of the cell. The source vector $\mathbf{H}$ is included in the vector $\mathbf{Q}$. The fluxes are computed at cell faces by averaging the cell-centre fluxes on adjacent sides. The finite volume scheme Eq. (6) constructed in this manner reduces to a central-difference scheme and is second-order accurate in space provided that the mesh is smooth enough. The vector $\mathbf{D}$ is the local dissipation flux required to eliminate spurious oscillations typical to central difference algorithm.

Artifical Dissipation

The cell centred spatial discretization method is non-dissipative so that any truncation and round-off errors are not damped in time, and oscillations may be present in steady-state solution. In order to eliminate these oscillations, dissipative terms $\mathbf{D}$ are added to Eq. (6). The dissipative term consists of the following operators in each direction:

$$D\mathbf{U}=D_x\mathbf{U}+D_r\mathbf{U} \qquad \ldots (7)$$

The dissipative fluxes in each direction are

$$D_x\mathbf{U}=d_{i+1/2,j}-d_{i-1/2,j}$$

$$D_r\mathbf{U}=d_{i,j+1/2}-d_{i,j+1/2}$$

$$d_{i+1/2,j}=\frac{(\Delta A)_{i+1/2,j}}{\Delta t}\{\varepsilon^{(2)}_{i+1/2,j}(\mathbf{U}_{i+1,j}-\mathbf{U}_{i,j})-\varepsilon^{(4)}_{i+1/2,j}(\mathbf{U}_{i+2,j}-3\mathbf{U}_{i+1,j}+3\mathbf{U}_{i,j}-\mathbf{U}_{i-1,j})\} \qquad \ldots (8)$$

These are of second- and fourth-order in the conserved variables, $\mathbf{U}$. The term $d_{i,j+1/2}$ and $d_{i,j-1/2}$ are calculated in an analogous manner. The numerical value of the constant ε influences the solution accuracy and, hence, must be carefully calculated. In this way, these ε coefficients are chosen so as to adapt them to the local flow gradients. The second order coefficient $\varepsilon^{(2)}$ calculated as

$$\varepsilon^{(2)}_{i+1/2ij}=\max(\nu_{i+1i},\nu_{i,j}) \qquad \ldots (9)$$

where.

$$\nu_{i,j}=\kappa^{(2)}\left|\frac{p_{i+1,j}-2p_{i,j}+p_{i-1,j}}{p_{i+1,j}+2p_{i,j}+p_{i-1,j}}\right| \qquad \ldots (10)$$

where $\kappa^{(2)}$ is a constant. However, the outcome is that $\varepsilon^{(2)}$ is positive, of order $(\Delta x)^2$, and proportional to the second difference of pressure. It supresses the oscillations around the shock. Fourth-order dissipation is added everywhere in the flow domain where the solution is smooth but are "switched-off" in the region of shock waves. The term involving second order differences is "switched-on" to damp oscillations near shock waves. The $\varepsilon^{(4)}$ is set to

$$\varepsilon^{(4)}_{i+1/2,j} = \max\{0, (\kappa^{(4)} - \varepsilon^{(2)}_{i+1/2,j})\} \quad \ldots (11)$$

where $\kappa^{(4)}$ is another constant. The scaling $[(\Delta A_{i+1/2,j})/\Delta t]$ in Eq. (8) confirms to the inclusion of the cell volume in the dependent variables of Eq. (6). Since Eq. (8) contains undivided differences, it follows that if $\varepsilon^{(2)} = 0(\Delta x)^2$ and $\varepsilon^{(4)} = 0(1)$, then the added terms are of $0(\Delta x)^3$, as will be the case in the regions where the flow is smooth. Near a shock wave $\varepsilon^{(2)}$ are in the range of 1 to 2, and $\kappa^{(4)}$ in the range of 1/32 to 1/256. In the present numerical analysis, various values of $\kappa^{(2)}$ and $\kappa^{(4)}$ are tried in order to control the numerical oscillations. the values of $\kappa^{(2)}$ and $\kappa^{(4)}$ are selected as 1.0 and 1/256, respectively.

Runge-Kutta Time-Stepping Scheme

The time dependent governing Eq. (6) is integrated numerically by means of the classical second-order Runge-Kutta method[10]. The following sequence of operations is used to obtain **U** at the time level n + 1 as;

$$\mathbf{U}^{n+1/2} = \mathbf{U}^n - 0.5\frac{\Delta t}{r_c \Delta A}\sum_{ij}[(\mathbf{F}_i \Delta r_i - \mathbf{G}_j \Delta x_j)\bar{r} - \mathbf{H}_{ij}A_{ij} - \mathbf{D}_{ij}] \quad \ldots (12a)$$

$$\mathbf{U}^{n+1} = \bar{\mathbf{U}}^n - \frac{\Delta t}{r_c \Delta A}\sum_{ij}[(\mathbf{F}_i \Delta r_i - \mathbf{G}_j \Delta x_j)\bar{r} - \mathbf{H}_{ij}A_{ij} - \mathbf{D}_{ij}] \quad \ldots (12b)$$

where Δt is the local time step, r_c the centroid of the cell, $\bar{r}$ the radial distance of the cell. The dissipative terms are frozen at their values in the first stage for second order Runge-Kutta scheme. The scheme is stable for a Courant number ≤ 1. Local time steps are used to accelerate convergence to a steady state solution by advancing the time-step at each point with the maximum time step allowed by the local CFL condition.

Boundary Conditions

The boundary conditions are enforced by using the idea of image cells at the centre line of the axisymmetric free jet.

At the nozzle exit, all of the flow properties are imposed since the incoming flow is supersonic.

At the downstream of the jet, all of the properties in the cell are extrapolated from the adjacent interior cells.

For quiescent external conditions, the ambient pressure is imposed as the outer boundary condition which is taken about 5 times the nozzle exit radius.

Experimental Procedure

All the tests were carried out in Open Jet Facility of VSSC. High pressure dry air at 4.3 MPa and ambient temperature was supplied through a 150 mm diameter pipe line to the settling chamber and nozzle assembly. A pressure regulating valve was used to control the nozzle operating pressure. The pressure in the settling chamber was continuously monitored using a Bourden pressure gauge and a pressure transducer. The facility can be operated continuously at the maximum pressure for about 80 s which is adequate for data acquisition.

The convergent-divergent nozzles were designed for producing supersonic free jets. The static pressure distribution in the axial direction of free jets was made using a miniature size stainless steel probe. The geometrical details of the nozzles and static probe are already described[11]. The probe is calibrated and is found to measure static pressure within ±1% of nominal value. A single-pass, black and white Schlieren system was employed for flow visualization photography.

Results and Discussion

Supersonic jets exhausting into a nominally stationary external stream are computed using inviscid solver. The initial jet radius is equal to exit nozzle radius. The outer boundary of the computational domain in the radial direction is located about 5 radius from the jet axis. In the stream wise direction, the calculation is carried out up to 20 jet radius. Due to the axisymmetric nature of the problem, computations have been made on one half of the jet. The image cell is taken while applying the symmetric condition on the centre line of the jet. The computations employed 600 equally spaced points in the axial direction. A grid refinement is carried out in the radial direction employing 80, 100 and 120 points. Grid inde-

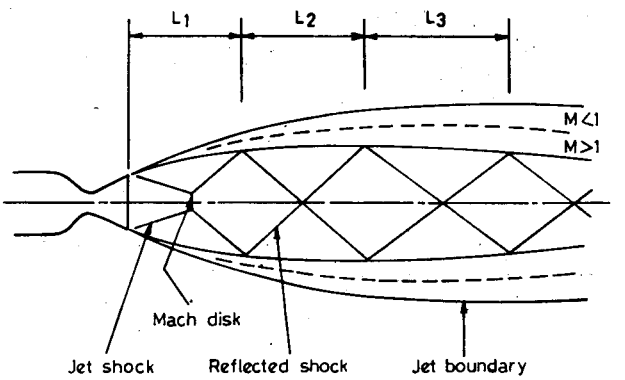

Fig. 1—Schematic sketch of a supersonic free jet

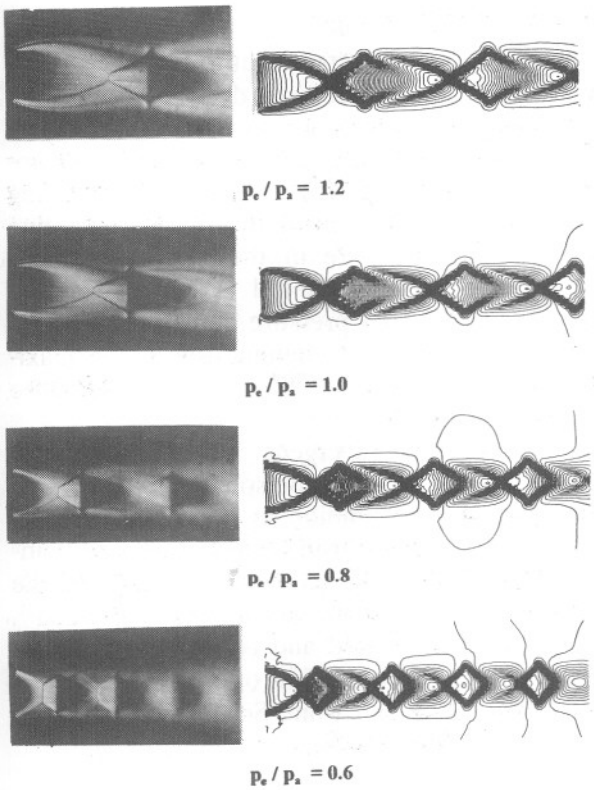

Fig. 2—Schileren photographs and pressure contours at different p_e/p_a for $M_e = 2.2$

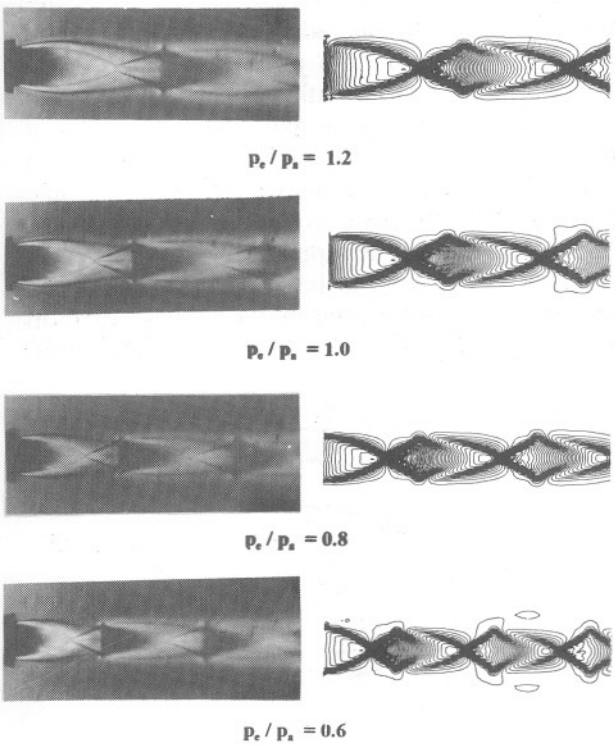

Fig. 3—Schileren photographs and pressure contours at different p_e/p_a for $M_e = 2.6$

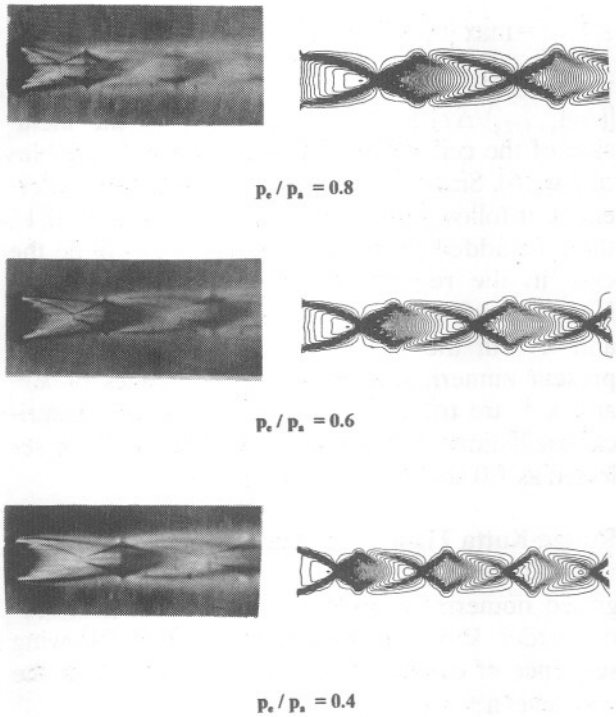

Fig. 4—Schileren photographs and pressure contours at different p_e/p_a for $M_e = 3.1$

pendent results are obtained for computations employing 120 points.

Shock cells—Fig. 1 illustrates, as an example, the underexpanded flow produced by a supersonic nozzle. Schlieren pictures of free jets and corresponding isobar contours at jet exit Mach number of 2.2, 2.6 and 3.1 at various jet exit to ambient pressure ratio (p_e/p_a) are depicted in Figs 2-4. The Schlieren pictures and isobar contours exhibits all the essential flow field features of the supersonic free jets, such as jet boundary, jet shock, Mach disk and reflected shock. The observations which can be made from the Schlieren pictures and isobar contours are that for a constant exit Mach number, the location of Mach disk moves closer to the nozzle exit plane and the length of the shock-cell length decreases with decrease in the exit to ambient pressure ratios. Moreover, the location of Mach disk moves away from the nozzle exit plane as the exit Mach number increases while taking same value of p_e/p_a.

The measured shock-cell lengths from the Schlieren pictures and isobar contours are displayed in Figs 5 and 6, and as L_1/d^* and L_2/d^* versus β^2, where β^2 is defined as

$$\beta^2 = \left(\frac{2}{\gamma-1}\right)\left(\frac{P_0}{p_a}\right)^{(\gamma-1)/\gamma} - \left(\frac{\gamma+1}{\gamma-1}\right) \quad \ldots (13)$$

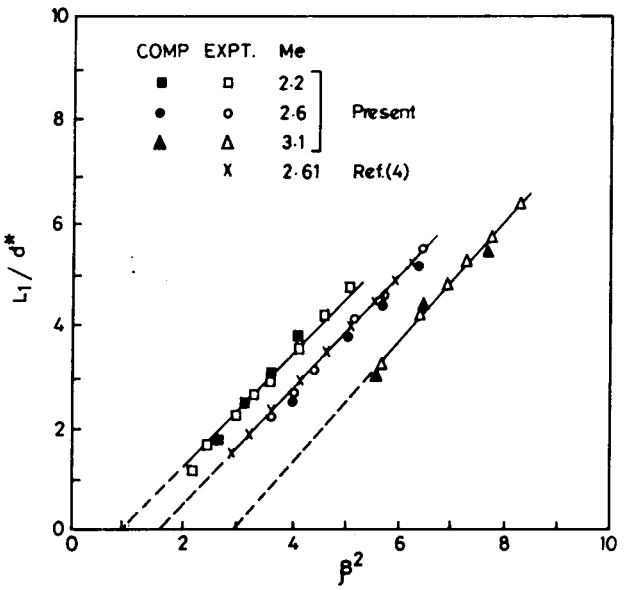

Fig. 5—Variation of first shock cell length L_1/d^* with β^2

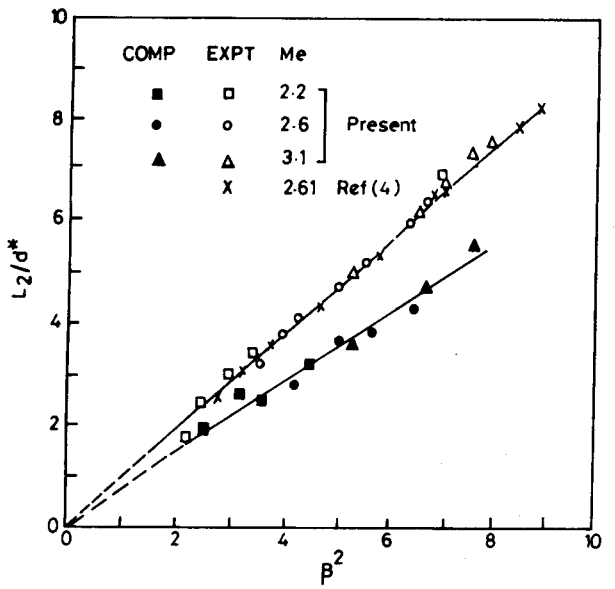

Fig. 6—Variation of second shock cell length L_2/d^* with β^2

The results in the figures indicate that a linear relationship can be established between them. The following linear relationship are obtained by applying least square fit to each nozzle:

$$L_1/d^* = 0.3(M_e + 1)\,\beta^2 - (2.75\,M_e - 5.2) \quad \ldots (14)$$

The validity of the constants are checked by direct comparison with the results of Abdel-Fattah[4] for $M_e = 2.6$ and found to be in good agreement. The comparisons between the present experimental and computed shock cell length are in good agreement.

It is observed from Schlieren pictures and isobar contours that in general first shock cell length

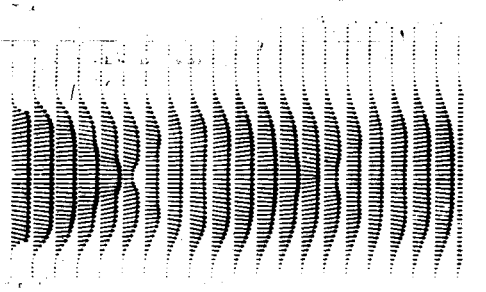

Fig. 7—Velocity vector plots in the jet for $M_e = 2.2$

is less than the second shock cell length for $p_e/p_a < 1$, and slope of the line decreases with decrease of the exit Mach number.

A linear relationship is obtained for the second shock cell length, L_2. The slopes of the best fit line are determined from computational and experimental results 0.72 and 0.87, respectively. The difference between them may be attributed to the faster jet spreading rate after first shock cell and hence the lower length of second shock-cell. However, the reason for the independency is not clear and needs further analysis. It is worth to mention here that the second shock cell length became independent of M_e.

The mechanism of generation of the broadband shock noise is due to the interaction between the fluctuating turbulence structures embaded in the convecting jet plume and the quasi-periodic shock-cell structure. When a supersonic jet is imperfectly expanded the pressure mismatch at the nozzle exit is adjusted by means of compression and expansion waves. These reflected compression waves converge to form a shock again raising the jet static pressure above ambient leading to another set of expansion waves. This process is repeated resulting in the repetitive shock structure as illustrated in Fig. 1. The viscous mixing taking place in the jet shear layer reduces the strength and spacing of these shock cells in the downstream direction. The eddies formed by this mixing process are convected downstream and interact with the shock cells to produce shock noise. The broadband shock associated noise spectrum can be computed using simple loop equation[12,13] which can be written as

$$f_p = n u_c/[L(1 + M_c \cos\theta)],\ n = 1, 2, 3, \ldots \quad \ldots (15)$$

where θ is the direction of noise measured from jet flow direction, u_c is the eddy convection velocity, L is the shock spacing, and $M_c = u_c/c_a$ with c_a equal to the ambient speed of sound. The disturbance convection velocity[4] can be assumed under acceptable condition as $u_c/U_j = 0.70 \pm 0.05$. The discrete tone fundamental frequency can be

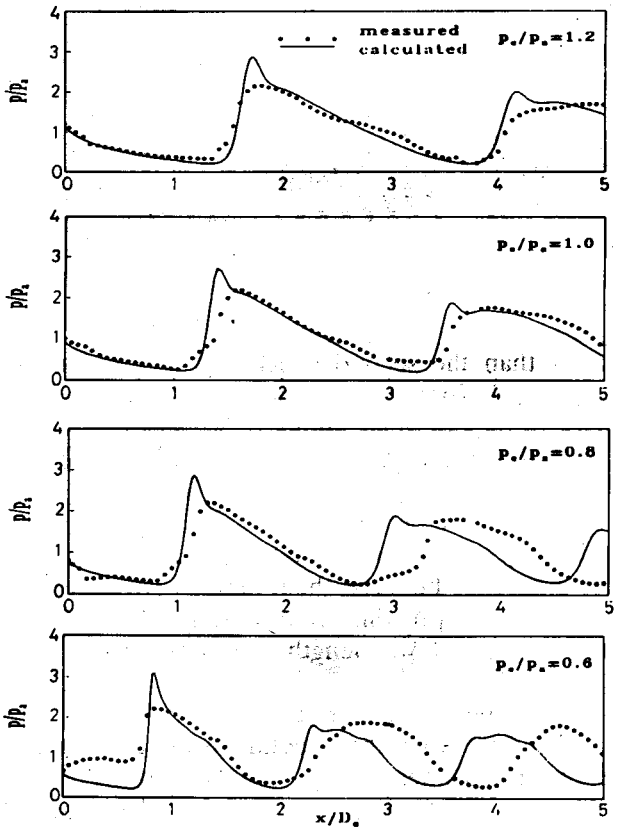

Fig. 8—Pressure variation along the jet axis for $M_e = 2.2$ at different p_e/p_a

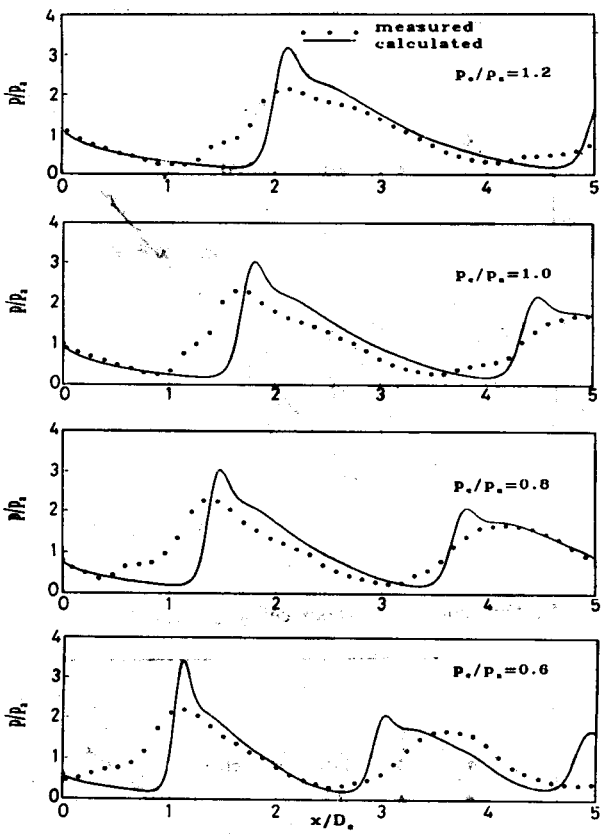

Fig. 9—Pressure variation along the jet axis for $M_e = 2.6$ at different p_e/p_a

calculated using Eq. (15) in conjunction with shock-cell length at the observer direction.

A glimpse of the computed velocity field in the jet is depicted in Fig. 7 for $M_e = 2.2$ and p_e/p_a. The velocity field depicts compression as well as expansion region of the free jets. The velocity profile clearly indicates that the velocity vector attains free stream condition smoothly at the jet boundary.

Static pressure along jet axis—Results obtained using the time marching code are compared to experimental static pressure measurements in the jets from three nozzles having exit Mach numbers of 2.2, 2.6 and 3.1. The data in Figs 8, 9 and 10 are shown normalized by the surrounding pressure p_a.

In Figs 8 and 9, the measured centre line pressure illustrates the decaying shock structure that occurs with jet spreading rates for the mildly underexpanded condition of $p_e/p_a = 1.2$ at $M_e = 2.2$ and 2.6. This condition corresponds to the illustrated flow field in Fig. 1. From these data it is evident that the shock strength rapidly decays with distance from the nozzle exit. Minimum pressure in Figs 8 and 9 correspond to the axial locations for shock reflection along the jet centre line, and the pressure maxima correspond to the end of a compression zone which is approximately the axial location where shocks terminate at the sonic line. The velocity field also reveals similar flow field features. Figs 8 and 9 show the general agreement between the measured static pressure and predicted by an inviscid code.

Also shown in Figs 8 and 9 are the centre line static pressure distribution for the $M_e = 2.2$ and 2.6 nozzle for what is commonly referred to as perfectly expanded flow (i.e., $p_e/p_a = 1.0$).

A typical examples of the code's prediction capability of overexpanded flow is shown in Figs 8 to 10 for $M_e = 2.2$, 2.6 and 3.1 nozzle with $p_e/p_a = 0.8$, 0.6 and 0.4. These figures display similar trend of pressure variation along the jet centre line. However, there is a difference between computational and experimental results, which may be attributed to faster jet spreading rate and inviscid analysis. The centre line distribution represents the axial extent of available data for these cases, and as is evident the code predicts the irregular-looking pressure data. The data show that there is good correspondence obtained for the location of

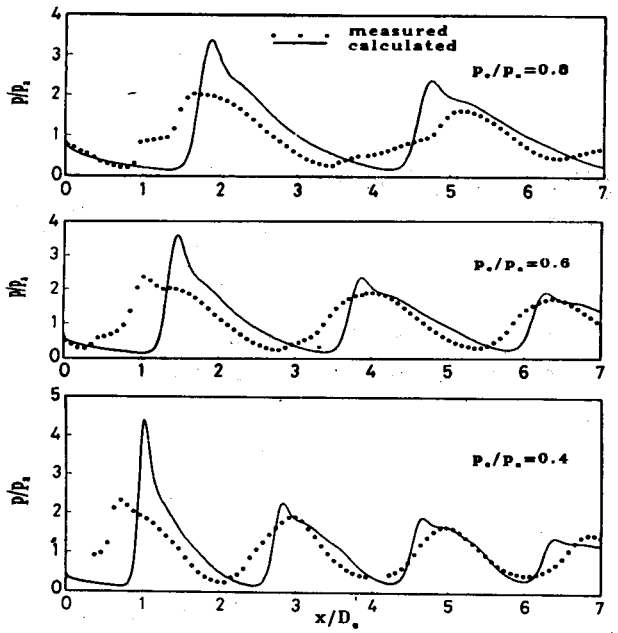

Fig. 10—Pressure variation along the jet axis for $M_c = 3.1$ at different p_e/p_a

the first three shock-cells. However, the amplitude for the first pressure maxima differs between measured and predicted results. It is known that the oblique shock strength is a strong functions of radial position as the sonic line is approached. Plume spreading could account for the small differences existing between measured and predicted results.

Conclusions

Experimental and numerical analyses are carried out for axisymmetric supersonic free jets emanating from conical convergent-divergent nozzles. The conclusions drawn from the analysis are that with the aid of Schlieren pictures and isobar contours, it is found that L_1/D^* varies linearly with β^2 but its coefficients depend on exit Mach number. The second shock cell length also displays linear dependency on β^2. However, it is noticed to be independent of exit Mach number. Moreover, the computed and measured centre line pressure variations are in good agreement upto 4 to 5 shock-cell length. However, in the case of overexpanded jet some disagreement with experimental data is noticed which is attributed to faster jet spreading rate.

Nomenclature

A = nozzle cross-sectional area
c_a = ambient speed of sound
d^* = nozzle diameter
e = total energy
f_p = shock noise peak frequency
$\mathbf{F}$ = vector of x-directed fluxes
$\mathbf{G}$ = vector of r-directed fluxes
$\mathbf{H}$ = source vector
I = internal energy
L = shock cell length
M = Mach number
M_c = convection Mach number of turbulent eddies
M_j = fully expanded jet Mach number corresponding to the isentropic expansion of jet from P_0
p = static pressure
P_0 = jet stagnation pressure
r = radial coordinate
t = time
T = temperature
$\mathbf{U}$ = vector of conserved variables
U_j = fully expanded jet velocity
u_c = disturbance convection velocity
u, v = velocity components
x = axial coordinate
β^2 = $(M_j^2 - 1)$
γ = ratio of specific heats
θ = observer angle with respect to the inlet axis
Δ = increment
ρ = density

Subscripts

a = ambient
e = nozzle exit
1,2 = first and second shock cell length, respectively

References

1 Love E S, Grigsby C E, Lee L P & Woodling M J, *Experimental and theoretical studies of axisymmetric free jets*, NASA TR-6, 1959.
2 Cheng S & Chow W C, *AIAAJ*, 12(8) (1974) 1079.
3 Tam C K W, Jackson J A & Seiner J M, *J Fluid Mech*, 153 (1985) 123.
4 Abdel-Fattah A M, *AIAAJ*, 26(3) (1988) 283.
5 Dash S M & Wolf D E, *Fully-coupled analysis of jet mixing problems, Part I: Shock-capturing model SCIPVIS*, NASA CR 3761, 1984.
6 Abdol-Hamid K S, *Three-dimensional calculations for underexpanded and overexpanded supersonic jet flows, Proc of the AIAA 7th Applied Aerodynamics Conference*, Seattle, Washington (1989) 289-293.
7 Sinha R, Zakky V & Erdos J, *AIAAJ*, 9(12) (1970) 2363.
8 Dash S M, Pearce B E & Pergament H S, *J Spacecraft Rockets*, 17(3) (1980) 190.
9 Zeeuw D D & Powell K G, *Euler calcualtions of axisymmetric under expanded jets by an adaptive-refinement method*, AIAA paper 92-0321, 1992.
10 Jameson A, Schmidt W & Turkel E, *Numerical simulation of the Euler equations by finite volume methods using Runge-Kutta time-stepping* schemes, AIAA paper No. 81-1259, 1981.
11 Mehta R C & Prasad J K, *Experimental and computational studies of high speed jet flows, Proc of the ASME/JSME, Fluid Engineering Annual Conference*, USA, Aug. 13-18 (1995) 139-144.
12 Powell A, On the mechanism of choked jet noise, *Proc Phys Soc, (London)* Section B, 66 (1953) 1039-1056.
13 Harper-Bourno M & Fisher M J, *The noise from shock waves in supersonic jets*, in Noise Mechanisms, AGARD CP-131, AGARD, Neuilly-Sur-Seine, France (1973) 11.1-11.13.